ASIA-PACIFIC SOLAR RESEARCH CONFERENCE
2016

Parameter study for design of flat tubular molten salt receivers

Meige Zheng, John Pye

Research School of Engineering, Australian National University, Canberra, Australia

E-mail: meige.zheng@anu.edu.au, john.pye@anu.edu.au

Abstract

The receiver is an essential part of a concentrating solar power (CSP) system, and its performance is strongly constrained by material limits which in turn limit the allowable flux on the receiver. This paper seeks to understand the benefits which arise at the receiver as a result of adjusting the flux profile, comparing a simple Gaussian 'spot' with a linear 'ramp' pattern, while respecting an upper limit on the allowable film temperature of the molten salt working fluid. The ramp profile performed better, matching material limits more closely over the receiver surface, hence permitting a smaller receiver with lower losses.

1. Background and literature review

Solar One and Solar Two [1] - [4] were the two pioneering central tower CSP systems, and operated in California between 1988 and 1999 respectively. Solar Two was a major re-vamp of Solar One with the addition of a molten salt receiver. Solar Tres (ultimately renamed 'Gemasolar') in Spain was the first commercial solar power plant built using this molten salt receiver technology, about three times the size of Solar Two, and commenced operation in April 2011 [5]. The 110 MWe SolarReserve Crescent Dunes system is the latest of this type.

Possible approaches to improve the efficiency of the receivers are reducing the surface temperature by varying the flux distribution, adopting the multi-diameter receivers and the

Nomenclature

h	convection coefficient, J/kg	T	temperature, °C
$\dot{Q}$	heat rate, MW	$\dot{X}$	exergy rate, MW
$\dot{W}$	energy rate, MW	α	absorptivity, solar-weighted
ϵ	emissivity	σ	Stefan-Boltzmann constant
n_{tubes}	No. of tubes per bank	n_{banks}	No. of tube banks in the receiver
n	No. of flow segments	G	direct normal irradiance, W/m^2
C	concentration ratio	L	length (along receiver tube), m
W	width, m	Nu	Nusselt number
k	thermal conductivity, W/(m·K)	Pr	Prandtl number
Re	Reynolds number	ρ	density, kg/m^3
f	friction factor	η	efficiency, %
V	Specific volume	Δp	pressure drop through receiver
$\dot{m}$	mass flow rate, kg/s		

Subscripts

spil	spillage	sun	total energy
inc	incident	refl	reflected
abs	absorbed	rad	radiation due to thermal emission
ext	external wall of receiver tube	int	internal wall of receiver tube
slice	for/in one flow segment only	conv	convective heat transfer
lost	lost through leaving the system	dest	destroyed within the system
i	Internal heat transfer to fluid	I	first law
II	second law	th/thermal	thermal
rec	receiver conditions	pu	pump conditions
PR	pump + receiver	i, o	Inlet/inside, outlet/outside

multi-pass receivers. Boerema et al. found that such techniques could improve energy efficiency by 1-2% [6]. Corrosion and thermal stress are the two most critical constraints in design of molten salt receivers, and were used to determine allowable flux density by Sánchez-González et al. [7]. This allowable flux density then leads to the need for accurate aiming strategies for the heliostat field.

In the optimization of concentrating solar systems, the second law of thermodynamics plays a significant role as it allows us to quantify the amount of work that can ultimately be extracted from a heat source (exergy), and deals with heat-transfer-related irreversibilities that act to reduce this amount [8]. Exergy analysis has proven to be a valuable tool to investigate possible configurations of the optimized solar thermal receivers, since it is able to present the types, causes and locations of thermodynamic losses more clearly when compared to energy analysis [9]. A review of exergy analysis on various types of solar collectors and applications of solar thermal systems was presented by Kalogirou et al. [10], emphasising its importance in the design of sustainable energy systems. The review includes exergetic analysis for various types of solar collectors including flat-plate collectors, hybrid PV/thermal systems, parabolic trough and dish collectors as well as other applications such as phase change materials.

2. Introduction

An exergy analysis of a 'Billboard' style tubular receiver, as shown in Figure 1, with different heat transfer fluids (HTF) was studied by Pye et al. [11]. It was shown that the performance of molten salt (with properties as per [12]) is highly competitive in its standard temperature range, but other fluids such as liquid sodium perform better if the temperature and solar flux concentration ratio can be increased. That study, however, considered only the case of uniform flux. This paper, as a further development, examines how non-uniform flux impacts the thermal performance.

The working temperatures of the molten salt are controlled within the range from 290℃ to 565℃. The lower limit is to avoid freezing, and the upper limit is to avoid chemical degradation of the salt. The present model is limited to flat/convex receivers. The flow path is separated into n sequential segments, with n_{banks} banks of parallel tubes passing up and down the receiver surface, connected together in series, with n_{tubes} parallel tubes in each bank. The value of n_{tubes} is calculated geometrically,

$$n_{\text{tubes}} = \frac{W}{d_o n_{\text{banks}}} \tag{1}$$

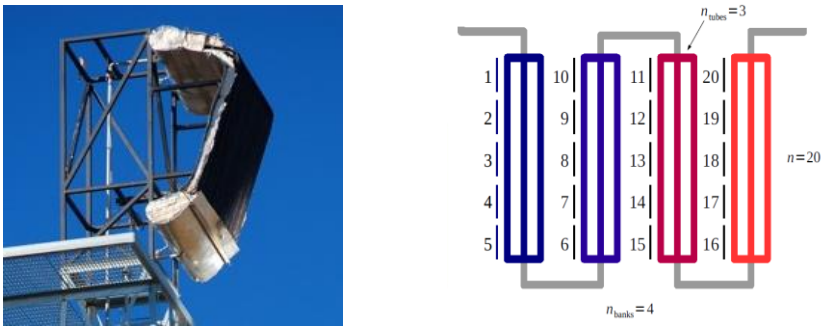

Figure 1. Left, a billboard receiver (Source: Vast Solar); right, the receiver pipe flow model, with segment numbering and flow-path configuration.

3. Methodology

The net energy flow into a receiver from concentrated solar radiation will be balanced by energy outflows from the flow of HTF or other energy conversion process, plus a range of energy losses, due to unwanted reflection, radiative emission, convective or conductive processes [13]. The total energy loss is the sum of these four contributions,

$$\dot{Q}_{\text{loss}} = \dot{Q}_{\text{inc}} - \dot{Q}_{\text{i}} = \dot{Q}_{\text{refl}} + \dot{Q}_{\text{rad}} + \dot{Q}_{\text{conv}} + \dot{Q}_{\text{cond}} \quad (2)$$

The first-law efficiency of thermodynamics indicates how well an energy transfer process is accomplished and provides a sound basis for studying the various forms of energy. The overall first-law efficiency of the receiver as well as the receiver thermal efficiency are

$$\eta_I = \frac{\dot{Q}_{\text{i}}}{\dot{Q}_{\text{sun}}} = \frac{\dot{m}[h(p_o,T_o)-h(p_i,T_i)]}{\dot{Q}_{\text{sun}}}, \text{ and} \quad (3)$$

$$\eta_{\text{th}} = \frac{\dot{Q}_{\text{i}}}{\dot{Q}_{\text{inc}}}, \text{ where } \dot{Q}_{\text{inc}} = \dot{Q}_{\text{sun}} - \dot{Q}_{\text{spil}} \quad (4)$$

As in the previous work, the exergy losses and exergy destruction (internal irreversibilities) in the receiver are accounted as follows:

$$\dot{X}_{\text{loss}} = \dot{X}_{\text{loss,refl}} + \dot{X}_{\text{loss,ext,rad}} + \dot{X}_{\text{loss,ext,rad}} + \dot{X}_{\text{loss,cond}} \quad (5)$$

$$\dot{X}_{\text{dest,tot}} = \dot{X}_{\text{dest,abs}} + \dot{X}_{\text{dest,wall}} + \dot{X}_{\text{dest,int,conv}} + \dot{X}_{\text{dest,flow}} \quad (6)$$

The overall second-law efficiency of the receiver is the ratio of the net increase in working fluid flow exergy to the exergy of the solar radiation reflected by the heliostat field,

$$\eta_{II} = \frac{\dot{X}_{\text{i}}}{\dot{X}_{\text{sun}}} \quad (7)$$

More detailed equations for energy and exergy balances are in the previous paper [11].

4. Simulation and parametric studies

4.1. Gaussian flux distribution

The distribution of irradiance on the receiver, assumed here to be flat, has been firstly approximated by a bivariate Gaussian distribution. A Gaussian spot is physically based and arises naturally when effects due to the sun-shape, heliostat slope errors and tracking errors are combined with a single-point aiming strategy. The Gaussian spot is represented by

$$G_{\text{rec}}(x,y) = \frac{\dot{Q}_{\text{sun}}}{2\pi\sigma^2} \exp\left(-\frac{1}{2}\left(\frac{r}{\sigma}\right)^2\right), \quad (8)$$

$$\text{where } r = \sqrt{\left(x-\frac{W}{2}\right)^2 + \left(y-\frac{L}{2}\right)^2} \quad (9)$$

and x and y are horizontal and vertical coordinates on the receiver of width W and height L.

For a given amount of $\dot{Q}_{\text{sun}}$ (here, 20 MW), the flux density map was set by the spot size (σ) and the geometry of the receiver. Spot size is affected by mirror quality, heliostat shape and the circumsolar ratio. Therefore, the parametric studies based on these factors have been presented in the following sub-sections.

Firstly, the effect of varied spot size σ on the thermodynamic efficiencies was studied. The Gaussian distribution was incorporated into the model as described in Section 2. The fraction

of solar flux incident on square targets of varying size, for varying σ, is shown in Figure 2. Smaller spots allow the solar flux to be collected with a smaller aperture, as expected.

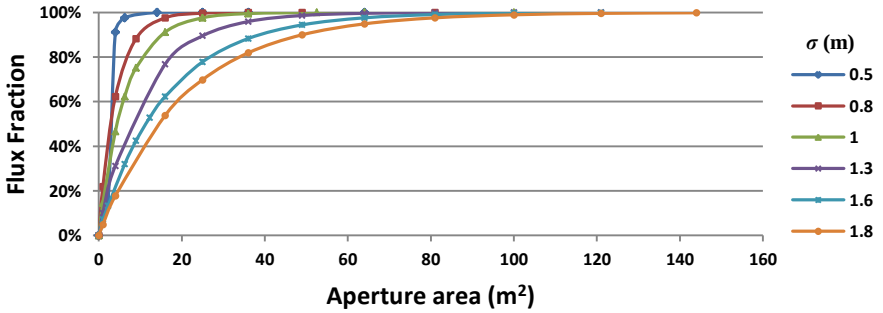

Figure 2. Flux distribution fraction vs. Aperture area of the receiver for different spot size, σ. Aperture is a square.

A small spot area is capable of performing high first-law efficiency due to the high peak flux density and low effect of spillage, as shown in Figure 3. The optimal spillage fraction here is ~5–8%, showing the strong trade-off between a small area with high spillage versus a large area with high thermal losses.

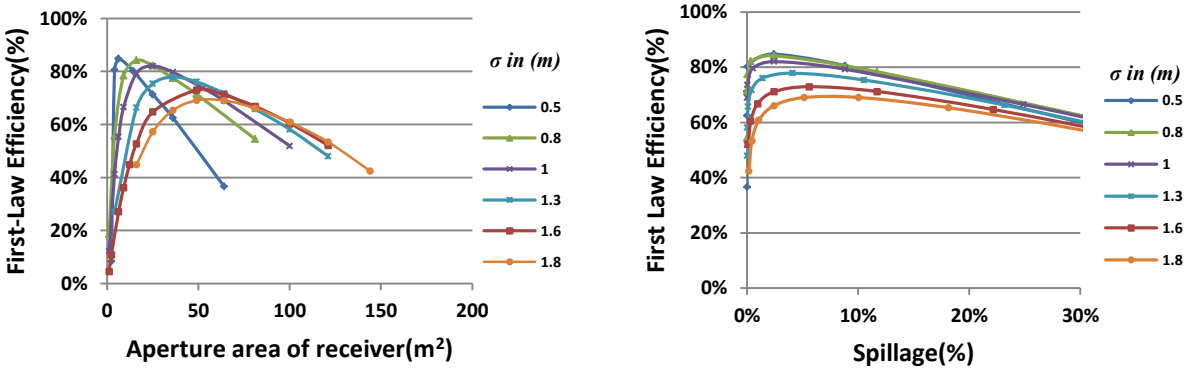

Figure 3. The effect of variable aperture areas and the spillage on the first law efficiencies.

Next, we studied the effect of the Gaussian spot size σ and the receiver aperture area A_{aper} on the peak film temperature $T_{film,peak}$ (Table 1). For small spots, very large peak film temperatures are seen, rendering the results above infeasible. González et al. [7] indicates that the highest allowable fluid temperature for molten salt should be 630℃. Therefore, the best-case σ and A_{aper} values were selected to be 1.9 m and 49 m^2 respectively for the remaining analysis.

Table 1. Peak film temperature $T_{film,peak}$ with spot size σ and A_{aper}.

σ, (m)	A_{aper} (m^2)	$T_{film,peak}$ (℃)	σ, (m)	A_{aper} (m^2)	$T_{film,peak}$ (℃)
0.5	6.25 - 64	1326 - 2240	0.8	16 - 81	960 - 1460
1.0	4 - 62	796 - 1058	1.3	4 - 64	744 - 825
1.6	16 - 81	648 - 740	1.9	36 - 64	620 - 643
2.1	64 - 81	619 - 636	2.3	25 - 64	608 - 610

Detailed exergy and energy accounting for molten salt receiver with variable σ and fixed A_{aper} (49 m^2) are presented in Figure 4 and Table 2. The dominant exergy destruction occurs

in the absorption step, due to the large step-down in temperature between the sun and the external walls of the receiver (from 5800 K to ~903.15 K (= 630℃)), decreasing a little for the case of very small spots. Spot size σ has a strong effect on spillage, as well as internal convection and external radiation. External radiation is sensitive to small areas of high external temperature, due to the T^4 effect. Internal convection losses arise from the large temperature difference between HTF and the inner wall (Figure 4). The trade-offs between spillage, external thermal radiation and internal convection lead to an optimal spot size with maximised total net exergy to the working fluid.

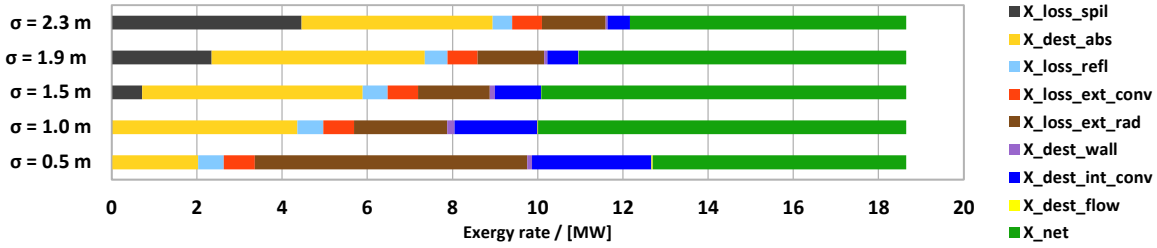

Figure 4. Exergy accounting for the receiver with varying spot size, for fixed aperture area (49 m²) and fixed total concentrated solar energy (20 MW).

Table 2. Effect of the size of a Gaussian spot on receiver performance.

Common parameters

$\dot{Q}_{\text{sun}}$	T_{sun}	P_{out}	k_{wall}	h_{ext}	T_{in}	T_{out}	G	A_{aper}	d_i	t	n_{banks}
20 MW	5800 K	1 bar	20 W/m·K	30 W/m^{2}K	290ºC	550ºC	1000 W/m^2	49 m^2	7 cm	1 mm	20

Results

σ	$\dot{Q}_{\text{inc}}$	$\dot{Q}_{\text{ref}}$	$\dot{Q}_{\text{ext,conv}}$	$\dot{Q}_{\text{ext,rad}}$	$\dot{Q}_{\text{i}}$	η_{th}	η_I	η_{II}	$T_{\text{int,peak}}$
m	MW	MW	MW	MW	MW	%	%	%	℃
0.5	20	0.6484	1.121	7.90	10.33	51.6	51.6	31.9	2090.11
1	19.95	0.6478	1.133	3.20	15.00	75.1	75.0	46.4	985.77
1.5	19.23	0.6235	1.132	2.60	14.88	77.4	74.4	47.8	702.66
1.9	17.48	0.5668	1.127	2.44	13.35	76.4	66.8	47.2	628.00
2.3	15.22	0.4934	1.120	2.35	11.26	74.0	56.3	45.7	597.78

The receiver temperature profiles (Figure 5) and the corresponding flux distributions (Figure 6) for these cases show that, for this particular flow configuration, the maximum inner wall temperature ($T_{\text{int,peak}}$) was 628℃, close to the allowable film temperature for molten salt, is reached when the spot size σ is set to 1.9 m. The peak flux density in that case is 0.87 MW/m^2. A larger value of σ, for example 2.3 m, results in excessive spillage.

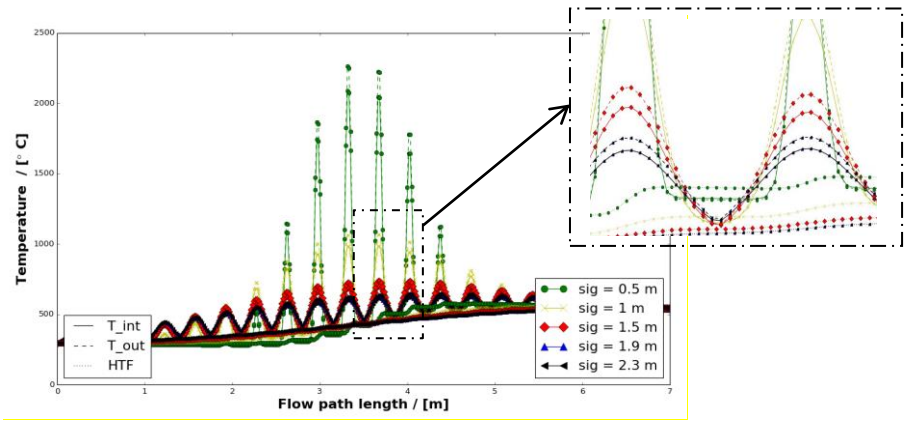

Figure 5 Receiver temperature profiles, for a range of spot sizes σ. Extracted detail is shown at top-right.

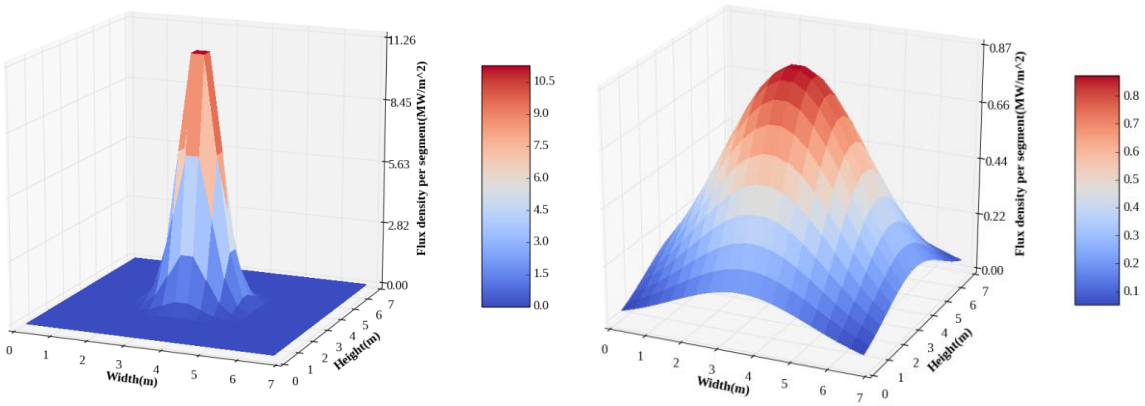

Figure 6. Gaussian flux profiles on a square 49 m² receiver: σ=0.5 m (left), σ=1.9 m (right).

4.2. Linear ramp flux distribution

In the above study we found that with Gaussian distribution, the maximum allowable film temperature is reached in only a small localised region, limiting the performance of the whole receiver. Therefore, it was proposed to examine whether a flux profile tailored to the rising fluid temperature could be shown to improve receiver performance. A simple linear ramp distribution in flux concentration was considered, with flux reducing from the left (inlet) to the right of the receiver surface (outlet), with the *x*-wise rate of reduction of flux (slope) being the variable parameter. This very simplified profile is similar to those arising from more detailed studies [7]. A sinusoidal curve is applied at the edges of this idealised flux profile, to mimic modest spillage losses. We adjusted the size of the aperture and the Concentration Ratio (CR) in order to match the peak film temperature constraint. The total flux and spillage are constant at 20 MW, 12% respectively.

The width here is defined as the rate of change of aperture irradiance $G_{\mathrm{rec}}(x,y)$ in the negative *x*-wise direction across the receiver. For the flat portion of distribution, exclusive the sinusoid 'tails",

$$\text{slope} = \frac{\Delta G_{\mathrm{rec}}(x,y)}{-\Delta x} \tag{10}$$

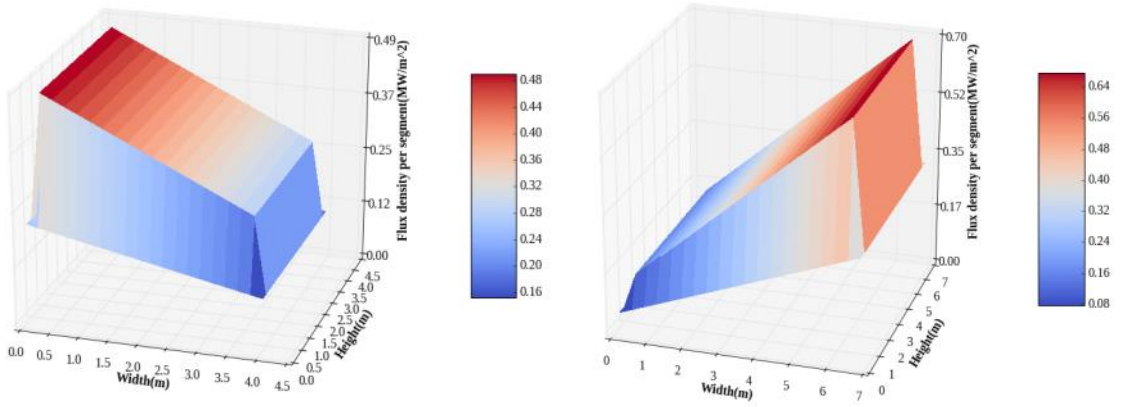

(a) (b)

Figure 7. Linear 'ramp' flux profiles: (a) slope +60 kW/m²/m, (b) slope –60 kW/m²/m.

The possible values of slope are from –125 to 125 kW/m^2/m when the lowest flux from that flat portion is set to be zero at the edge of the receiver.

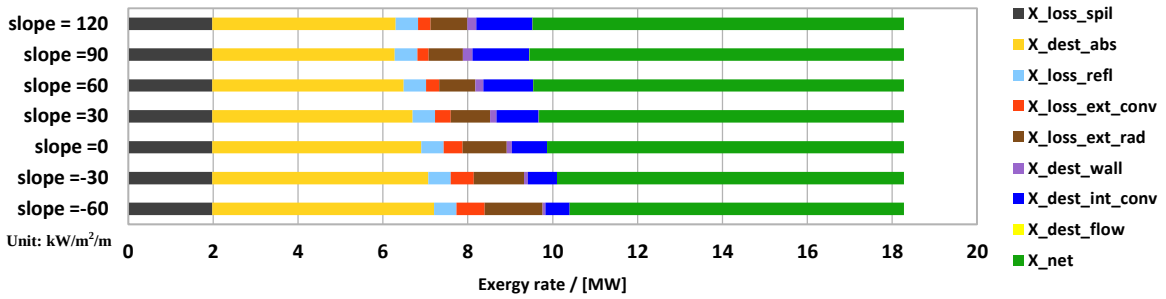

Figure 8 Exergy accounting with variable slope (in kW/m²/m).

$T_{\text{int\_peak}}$ were fixed at 630℃ by varying the size of aperture and the CR.

Results for the ramp flux profile study show that, for fixed aperture area, the negative slope (higher flux at outlet) cases perform worse than positive slope cases (higher flux at inlet). The negative slope cases (slope from –60 to –125 kW/m^2/m) lead to the maximum film temperature constraint being broken. When positive slope cases are used, and the aperture area is adjusted until the peak film temperature equals the maximum allowable value, smaller receivers with higher efficiency result. Even though the external surface temperatures are higher, the reduced area gives overall lower losses. The best case found was with a slope of 90 kW/m^2/m, since it had the smallest aperture of 13.9 m^2 which resulted in lowest exergy destroyed in absorption step.

4.3. Effect of tube diameter

We used Gaussian distribution as an example to study the effects of varying other major parameters on the thermodynamic efficiencies since the trends for these efficiencies are the same in the cases of Gaussian distribution and Linear distribution. The optimal spot size σ (1.9 m) was determined in Section 4.1.

To start with the tube inside diameter, decreasing tube diameter lowers the inner and outer wall temperatures, since a smaller tube gives higher fluid velocity, resulting in increased Reynolds number, and hence increased Nusselt number and improved internal heat transfer coefficient (Figure 10). The result is reduced exergy destruction in internal convection and reduced external losses. Results for a Gaussian flux profile (Figure 9, Table 3).

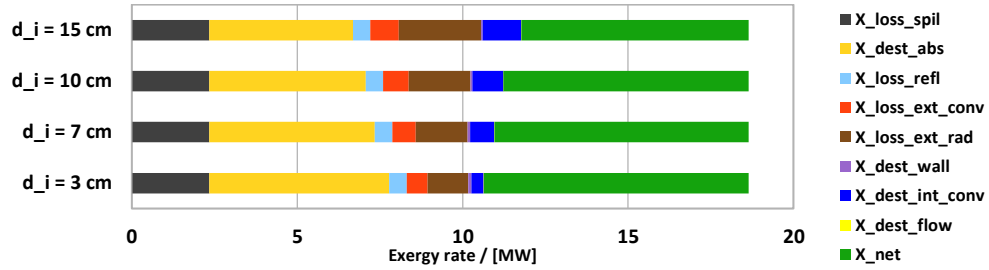

Figure 9. Exergy accounting with variable d_i (Gaussian Flux profile).

There is no optimal tube diameter identified by the model at this stage, since the results shows that the receiver efficiency keeps increasing as tube diameter decreases.

The Prandtl number Pr, a material parameter, is the ratio of diffusivities of momentum and temperature. If the d_i is too small, Pr number would be out of its lower bound which is 0.6 for the Dittus-Boelter internal convection correlation used here. This limits the smallest d_i to be 3

cm is this case study. Also, if d_i becomes too small, it also causes excessive pressure drops (Δp).

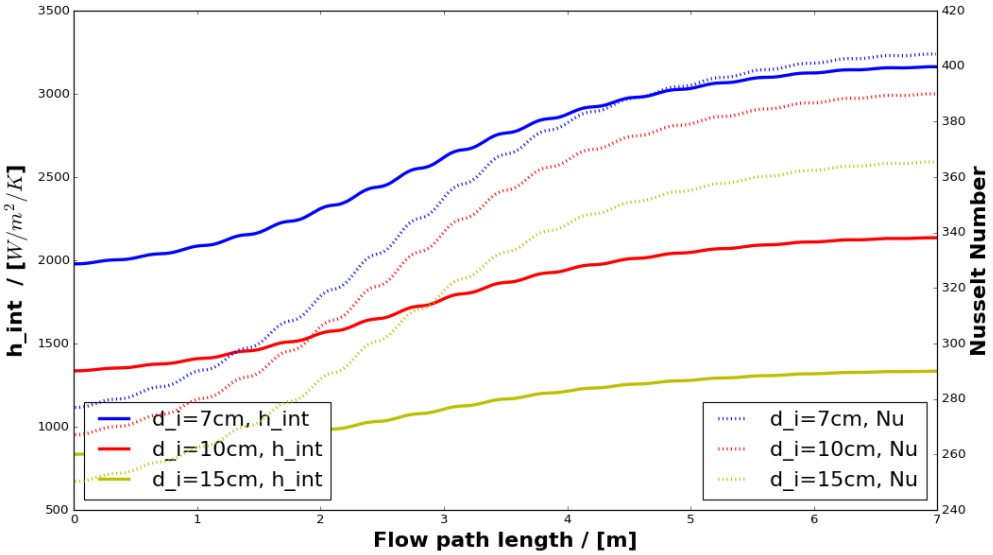

Figure 10. Trends in internal heat transfer (h_{int}, Nu) with varied internal diameter d_i.

Table 3. Effect of tube diameter d_i, with a Gaussian flux profile.

Common parameters

$\dot{Q}_{\text{sun}}$	T_{sun}	P_{out}	k_{wall}	h_{ext}	T_{in}	T_{out}	G	A_{aper}	t_{wall}	σ	n_{banks}
20 MW	5800 K	1 bar	20 W/m·K	30 W/m^{2}K	290ºC	550ºC	1000 W/m^2	49 m^2	1 mm	1.9 m	20

Results

d_i	$\dot{Q}_{\text{inc}}$	$\dot{Q}_{\text{ref}}$	$\dot{Q}_{\text{ext,conv}}$	$\dot{Q}_{\text{ext,rad}}$	$\dot{Q}_{\text{i}}$	η_{th}	η_I	η_{II}	$T_{\text{int,peak}}$
cm	MW	MW	MW	MW	MW	%	%	%	℃
3	17.48	0.57	1.040	1.969	13.91	79.5	69.5	49.1	566.6
7	17.48	0.57	1.127	2.437	13.35	76.4	66.8	47.2	626.37
10	17.48	0.57	1.192	2.855	12.87	73.6	64.3	45.5	685.93
15	17.48	0.57	1.297	3.677	11.94	68.3	59.7	42.1	771.56

4.4. Effect of tube wall thickness

Reducing the tube wall thickness has the expected effect of improving receiver performance by reducing the thermal resistance of the wall and hence exergy destruction in the wall as well as lowering external temperatures and the corresponding thermal losses. A secondary effect is that thinner tube length allow an increase in the total pipe length, allowing a slightly increase in n_{tubes} per bank, even allowing non-integer values. Results are shown in Table 4.

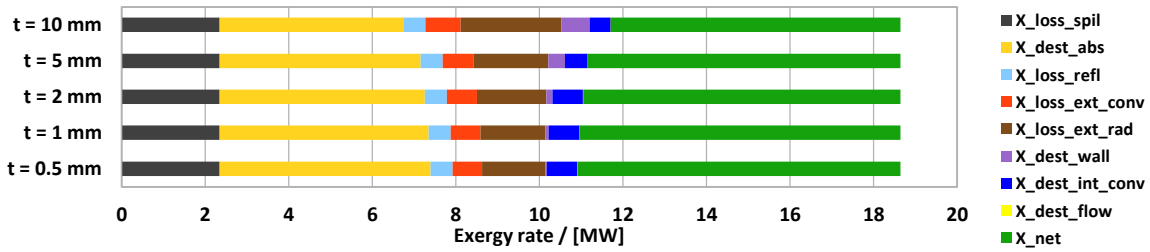

Figure 11. Exergy accounting with the changing tube thickness t (Gaussian flux profile).

Table 4 Effect of tube wall thickness t (Gaussian flux profile).

Common parameters

$\dot{Q}_{sun}$	T_{sun}	P_{out}	k_{wall}	h_{ext}	T_{in}	T_{out}	G	A_{aper}	d_i	σ	n_{banks}
20 MW	5800 K	1 bar	20 W/m·K	30 W/m^{2}K	290ºC	550ºC	1000 W/m^2	49 m^2	7 cm	1.9 m	20

Results

t_{wall}	$\dot{Q}_{inc}$	$\dot{Q}_{ref}$	$\dot{Q}_{ext,conv}$	$\dot{Q}_{ext,rad}$	$\dot{Q}_i$	η_{th}	η_I	η_{II}	$T_{int,peak}$
mm	MW	MW	MW	MW	MW	%	%	%	℃
0.5	17.48	0.57	1.117	2.373	13.42	76.8	67.1	47.4	627.96
1	17.48	0.57	1.127	2.437	13.35	76.4	66.8	47.2	628.00
2	17.48	0.57	1.148	2.570	13.20	75.5	66.0	46.6	628.01
5	17.48	0.57	1.172	2.738	13.00	74.4	65.0	45.9	628.53
10	17.48	0.57	1.282	3.584	12.05	68.9	60.2	42.6	627.49

4.5. Effect of flow configuration

The flow configuration shown in Figure 1 allows varying degrees of flow in parallel or in series. By increasing n_{banks}, the flow path lengthens and there are less tubes in parallel. The model excludes tube-end manifolds and minor losses, but the important effects of tube friction and heat transfer enhancement, due to varying fluid velocities in the different configurations, are captured. Results below (Figure 12 and Table 5 for Gaussian profile; Figure 13 and Table 6 for linear profile) show the effect of changing n_{banks}. Similar to the scenario of varying the tube diameter, a larger number of banks causes reduced external radiation and internal convection exergy destruction, resulting in higher overall efficiency, driven by improved internal convection. If n_{banks} were large, however, the tube wall thickness t would need to be increased to avoid excessive hoop stress in the tubes (this model requires a safety factor on hoop stress of at least one compared to an allowable stress fixed constant at 100 MPa), but at this stage t was kept constant and n_{banks} were less than 80.

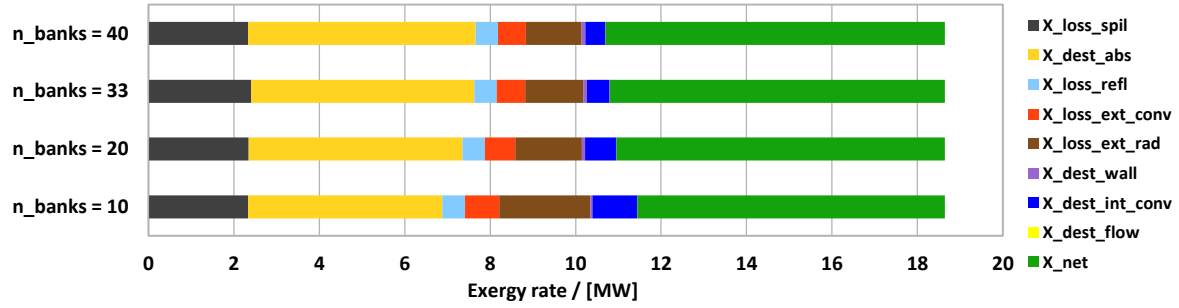

Figure 12. Exergy accounting with changing n_{banks} (Gaussian flux profile).

Table 5. Effect of flow configuration (Gaussian flux profile).

Common parameters

$\dot{Q}_{sun}$	T_{sun}	P_{out}	k_{wall}	h_{ext}	T_{in}	T_{out}	G	A_{aper}	d_i	t_{wall}
20 MW	5800 K	1 bar	20 W/m·K	30 W/m^{2}K	290ºC	550ºC	1000 W/m^2	49 m^2	7 cm	1 mm

Results

n_{banks}	$\dot{Q}_{inc}$	$\dot{Q}_{ref}$	$\dot{Q}_{ext,conv}$	$\dot{Q}_{ext,rad}$	$\dot{Q}_i$	η_{th}	η_I	η_{II}	$T_{int,peak}$
-	MW	MW	MW	MW	MW	%	%	%	℃
10	17.48	0.57	1.240	3.200	12.49	71.38	62.45	44.08	734.84
20	17.48	0.57	1.127	2.437	13.35	76.37	66.75	47.16	626.37
33	17.48	0.57	2.152	2.152	13.62	78.22	68.11	48.30	586.37
40	17.48	0.57	2.076	2.076	13.79	78.83	68.97	48.68	576.65
80	17.48	0.57	1.03	1.91	13.97	80.17	70.47	49.51	558.88

Table 5 shows that highest performance is obtained with highly in-series flow (n_{banks} = 80), when the flux profile is Gaussian. Next, we considered the same optimal linear flux distribution in Section 4.2 (slope, 90 kW/m^2/m) and again considered variables in n_{banks}. Results are presented in Figure 13 and in Table 6. Again it shows the n_{banks} = 80 gives the best performance.

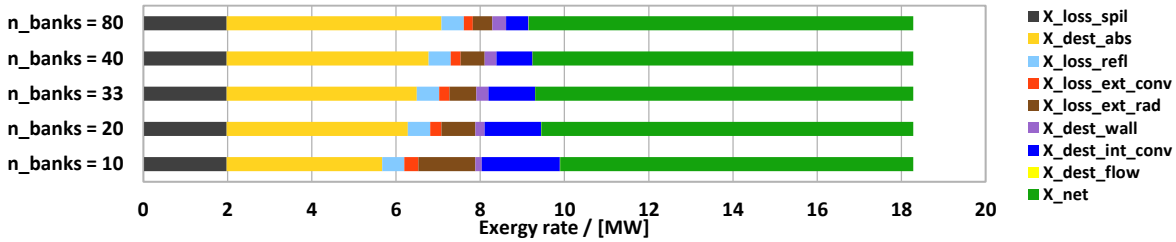

Figure 13. Exergy accounting with effect of variable n_{banks} (Linear profile)

Table 6. Receiver performance for Linear flux profile with varying flow configuration

Common parameters

$\dot{Q}_{\text{sun}}$	T_{sun}	P_{out}	k_{wall}	h_{ext}	T_{in}	T_{out}	G	A_{aper}	d_i	t_{wall}
20 MW	5800 K	1 bar	20 W/m·K	30 W/m^{2}K	290ºC	550ºC	1000 W/m^2	13.9 m^2	7cm	1 mm

Results

n_{banks}	$\dot{Q}_{\text{inc}}$	$\dot{Q}_{\text{ref}}$	$\dot{Q}_{\text{ext,conv}}$	$\dot{Q}_{\text{ext,rad}}$	$\dot{Q}_{\text{i}}$	η_{th}	η_I	η_{II}
-	MW	MW	MW	MW	MW	%	%	%
10	17.48	0.57	0.470	1.891	14.554	83.25	72.77	51.41
20	17.48	0.57	0.400	1.183	15.333	87.80	76.66	54.16
33	17.48	0.57	0.369	0.966	15.581	89.12	77.90	55.03
40	17.48	0.57	0.358	0.872	15.685	89.72	78.42	55.40
80	17.48	0.57	0.335	0.732	15.849	90.66	79.24	55.98

4.6. Discussion on pumping losses

The above studies suggest that tubes with a large number of banks with very small thin tubes will be the most efficient, were it not for limits due to tube stresses and perhaps limits on manufacturability. Both decreased d_i and increased n_{banks} however will increase the receiver pressure drop Δp, resulting in presumably much increased pumping work. Therefore, a pump is implemented into the modelling to re-calculate the thermodynamic efficiencies and exergy destruction. As molten salt is modelled here as an incompressible fluid, and assuming negligible temperature rise across the pump, we can relate the isentropic efficiency of the pump to the pump work (defined to be negative when system is doing work on the pump) using

$$\eta_{\text{is}} = \frac{\dot{m}\mathbf{V}_i(p_i - p_o)}{\dot{W}_{\text{pump}}} \quad (11)$$

Now, the thermodynamic efficiencies of overall system (pump + receiver) are defined here as:

$$\eta_{I,\text{PR}} = \frac{\dot{Q}_{\text{i}}}{\dot{Q}_{\text{sun}} - \dot{W}_{\text{pump}}} \frac{\dot{m}[h(p_{o,\text{rec}}, T_{o,\text{rec}}) - h(p_{i,\text{pu}}, T_{i,\text{pu}})]}{\dot{Q}_{\text{sun}} - \dot{W}_{\text{pump}}} \quad (12)$$

$$\eta_{\text{th,PR}} = \frac{\dot{Q}_{\text{i}}}{\dot{Q}_{\text{inc}} - \dot{W}_{\text{pump}}} \quad (13)$$

$$\eta_{II,\text{PR}} = \frac{\dot{X}_{\text{i,rec}} + \dot{X}_{\text{i,pu}}}{\dot{X}_{\text{sun}} - \dot{W}_{\text{pump}}} \quad (14)$$

Using Gaussian flux distribution and varied n_{banks} as an example, we now discuss the effect of the pump on these efficiencies. A $\dot{W}_{\text{pump}}$ of 48.19 kW is required to supply a HTF with pressure in 20.86 bar. This amount of energy required is negligible when compared with other exergy losses and destructions. This was evident from thermodynamic efficiency results listed in Table 7. As can be seen, pump work has no significant effect on the thermal efficiencies.

Table 7. Effect of variable n_{banks} when pump was implemented into the system

Results (cont'd Table 5)

n_{banks} -	η_{th} %	η_I %	η_{II} %	$\eta_{\text{th,PR}}$ %	$\eta_{I,\text{PR}}$ %	$\eta_{II,\text{PR}}$ %	W_{pump} kW	Δp bar
10	71.383	62.451	44.079	71.383	62.451	44.079	-0.107	0.05
20	76.367	66.750	47.157	76.367	66.750	47.157	-0.872	0.38
30	78.223	68.106	48.303	78.223	68.106	48.303	-3.72	1.57
40	78.828	68.965	48.677	78.828	68.965	48.677	-6.59	2.75
80	80.171	70.473	49.506	80.170	70.473	49.505	-48.19	19.86

5. Conclusion and discussion

From these case studies, the trends of thermodynamics efficiencies for individual conditions have been found. A comparison between best-case Gaussian and linear flux distributions is summarised in Table 8. Results show that the linear flux distribution is able to improve the efficiencies by ~ 10%, when compare with Gaussian distribution. It evidently shows the benefits of linear flux distribution, especially in the context of restriction in elevated temperatures and being able to tolerate higher flux densities. In addition to the effect of flux profile, effects of tube diameter, thickness and flow configuration were examined, and it was shown that in the absence of more detailed models of material constraints, the most efficient molten salt receivers have a large number of thin small-diameter pipes running mostly in series.

Table 8. Summary comparison of best-case designs for Gaussian and Linear flux profiles

Common parameters

$\dot{Q}_{\text{sun}}$	T_{sun}	P_{out}	k_{wall}	h_{ext}	T_{in}	T_{out}	G	d_i	t
20 MW	5800 K	1 bar	20 W/m·K	30 W/m^{2}K	290ºC	550ºC	1000 W/m^2	7 cm	1 mm

Results

Flux	$\dot{Q}_{\text{inc}}$ MW	$\dot{Q}_{\text{ref}}$ MW	$\dot{Q}_{\text{ext,conv}}$ MW	$\dot{Q}_{\text{ext,rad}}$ MW	$\dot{Q}_{\text{i}}$ MW	η_{th} %	η_I %	η_{II} %	A_{aper} m^2
Gaussian (from Table 5)	17.48	0.57	1.03	1.91	13.97	80.17	70.47	49.51	49
Linear (from Table 6)	17.48	0.57	0.335	0.732	15.85	90.66	79.24	55.98	13.9

6. Future work

Many areas for future work exist, including a more extensive optimisation process and more thorough consideration of material constraints on the receiver performance. Results will be generalised to the case of non-convex receivers, specifically bladed receivers. Tube expansion and minor losses will also be considered. More accurate flux profiles based on detailed ray-tracing will be integrated with the model.

Acknowledgements

Funding from the Australian Renewable Energy Agency (grant 2014/RND0101-UFA006) is gratefully acknowledged.

References

[1] G.J. Aubrecht, 'Extension 21.6: Solar One and Solar Two' from Ch. 21 of *Energy: Physical, Environmental and Social Impact*, 3rd Ed., Prentice Hall.

[2] C.E. Tyner, J.P. Sutherland, and W.R. Gould, 1995. 'Solar Two: A Molten Salt Power Tower Demonstration'. Technical report SAND95-1828C, Sandia National Laboratories.

[3] Sun Lab (2000). 'Solar Two Demonstrates Clean Power for the Future'. Fact sheet SAND2000-0613, http://www.nrel.gov/docs/legosti/fy97/22835.pdf, Accessed 11 Nov 2016.

[4] M. Romero, R. Buck, and J.E. Pacheco, 2002. 'An update on solar central receiver systems, projects and technologies' *J. Sol. Energy Eng.* **124(2)**, pp. 98-108.

[5] SolarPACES, 2016. 'Gemasolar Thermosolar Plant' (from the NREL Concentrating Solar Power Projects database) http://www.nrel.gov/csp/solarpaces/project_detail.cfm/projectID=40. Accessed 11 Nov 2016.

[6] N. Boerema, G. Morrison, R. Taylor, and G. Rosengarten, 2013. 'High temperature solar thermal central-receiver billboard design'. *Sol. Energy* **97** pp. 356-368

[7] A. Sánchez-González, M.R. Rodríguez-Sánchez, and D. Santana, 2016. 'Aiming strategy model based on allowable flux densities for molten salt central receivers'. *Sol. Energy* (in press).

[8] Y.A. Çengel and M.A. Boles, 2011. *Thermodynamics: An Engineering Approach*, 7th SI Ed, McGraw-Hill.

[9] I. Dincer and T.A.H. Ratlamwala, 2013. 'Importance of exergy for analysis, improvement, design, and assssment' *WIREs Energy Environ.* 2(3) pp. 335–349.

[10] S. A. Kalogirou, S. Karellas, V. Badescu, and K. Braimakis (2015) 'Exergy analysis on solar thermal systems: A better understanding of their sustainability' *Renew. Energ.* **85** pp.1328–1333.

[11] J. Pye, M. Zheng, J. Zapata, C.-A. Asselineau, and Coventry, 2014. 'An exergy analysis of tubular solar-thermal receivers with different working fluids' In *Proceedings of SolarPACES 2014*, Beijing.

[12] A.B. Zavoico, 2001. 'Solar Power Tower Design Basis Document'. Technical report SAND2001-2100, Sandia National Laboratories, Albuquerque.

[13] K. Lovegrove and J. Pye, 2012. 'Fundamental Principles of concentrating solar power (CSP) systems', In *Concentrating solar power technology: principles, developments and applications* (Eds. K. Lovegrove and W. Stein), Woodhead Publishing, Cambridge, UK.

[14] https://en.wikipedia.org/wiki/Normal_distribution, 'The probability density of the normal distribution' (2016). Retrieved 1 Nov 2016.